Raman spectra of cubic and amorphous $Ge_2Sb_2Te_5$ from first principles

Gabriele C. Sosso,[1] Sebastiano Caravati,[2] Riccardo Mazzarello,[2,3] and Marco Bernasconi[1,*]

[1]*Dipartimento di Scienza dei Materiali, Universitá di Milano-Bicocca, Via R. Cozzi 53, I-20125 Milano, Italy*

[2]*Computational Science, Department of Chemistry and Applied Biosciences, ETH Zurich, USI Campus, via Giuseppe Buffi 13, CH-6900 Lugano, Switzerland*

[3]*Institute for Theoretical Solid State Physics and JARA–Fundamentals of Future Information Technology, RWTH Aachen, D-52056 Aachen, Germany*

(Received 4 November 2010; revised manuscript received 25 February 2011; published 11 April 2011)

We computed the Raman spectrum of cubic and amorphous $Ge_2Sb_2Te_5$ (GST) by *ab initio* phonons and an empirical bond polarizability model. Models of the amorphous phase were generated by quenching from the melt by means of *ab initio* molecular dynamics simulations. The calculated spectra are in good agreement with experimental data which confirms the reliability of the models of the amorphous phase emerged from the simulations. All the features of the spectrum in both crystalline and amorphous GST can be assigned to vibrations of defective octahedra. The calculations reveal that the polarizability of the Sb-Te is much higher than that of Ge-Te bonds and of Ge-Ge/Sb wrong bonds resulting in a much lower Raman response of tetrahedra which are made of Ge-Te and wrong bonds. As a consequence and as opposed to amorphous GeTe, the signatures of tetrahedra in the Raman spectrum of amorphous GST are hidden by the larger Raman cross section of defective octahedra.

DOI: 10.1103/PhysRevB.83.134201 PACS number(s): 61.43.Bn, 61.43.Dq, 63.50.−x

I. INTRODUCTION

Phase-change materials (PCM) based on chalcogenide alloys are of great technological importance due to their ability to undergo a fast and reversible transition between the amorphous and crystalline phases upon heating.[1] This property is exploited in rewritable optical media (DVDs) and electronic nonvolatile memory (NVM), which are based on the strong optical and electronic contrast between the two phases.[1–3]

$Ge_2Sb_2Te_5$ (GST) is presently the material of choice for applications in NVM due to its superior performances in terms of crystallization speed and data retention. However, depending on the preparation conditions different amorphous phases exist with different crystallization speeds.[4] Although the amorphous structures generated by different means such as rf sputtering or ion irradiation have a very similar diffraction pattern, they can be discriminated by Raman spectroscopy.[5] With this aim, an assignment of the Raman spectra of amorphous GST (a-GST) has been proposed[5] on the basis of the structural model introduced by Kolobov *et al.* from the analysis of x-ray absorption fine structure (EXAFS).[6,7] The average coordination of Ge atoms inferred from EXAFS data decreases from sixfold in the crystal to a fourfold coordination in both a-GST and a-GeTe. Consequently, the Raman spectra of a-GST and a-GeTe have been interpreted in terms of vibrations of $GeTe_{4-n}Ge_n$ tetrahedra (where $n = 0, \ldots, 4$).[8,9] However, while a fourfold coordination can be reliably inferred from EXAFS, bonding angles are subject to large uncertainties. Recent *ab initio* molecular-dynamics simulations[10–15] of a-GST and a-GeTe showed that indeed Ge atoms are mostly fourfold coordinated in the melt-quenched amorphous phases, but only approximately one-third of Ge atoms display tetrahedral coordination (one-fourth in a-GeTe), whereas the majority of Ge and all Te and Sb atoms are in defective octahedra with bond angles typical of the octahedral geometry ($\sim 90^\circ$ and $\sim 180^\circ$) but with coordination lower than six. Moreover, three Ge-Te or Sb-Te bonds in defective octahedra are shorter than the others giving rise to a $3 + n$ coordination which, as recently pointed out by Xu *et al.*,[16] is ruled by the formation of p bonds. In a recent work[15] we have shown that the theoretical model of a-GeTe generated by quenching from the melt correctly reproduces the experimental Raman spectrum.[8,9] Although signatures of tetrahedral Ge can be identified in weak Raman features above 190 cm^{-1}, the most prominent peaks in the Raman spectrum of a-GeTe are mainly due to vibrations of atoms in defective octahedral sites as opposed to the experimental assignment of Refs. 8,9, in which the coexistence of tetrahedral and octahedral sites was overlooked.

In this work, we extend our *ab initio* investigation of Raman spectra to GST, aiming also at elucidating the source of a rather unusual feature of GST which shows much broader Raman peaks and a larger spectral range in the crystalline phase than in the amorphous phase.

II. COMPUTATIONAL DETAILS

We used models of a-GST generated by quenching from the melt within *ab initio* molecular dynamics simulations. We considered the 270-atom model discussed in Ref. 11. The metastable cubic GST (c-GST) was modeled by a supercell with 270 atoms in the rocksalt geometry where Te occupies one sublattice while Ge, Sb, and 20% of vacancies are randomly placed in the other sublattice at the experimental lattice parameter (6.02 Å) of c-GST,[17] as reported in Ref. 11.

As in our previous work on a-GeTe,[15] the Raman spectra of the GST models were calculated from *ab initio* phonons and empirical polarizability coefficients within the bond polarizability model (BPM).[18] *Ab initio* calculations based on density functional theory were performed in the same framework used in our previous works.[10,11] The Perdew-Burke-Ernzerhof (PBE)[19] exchange-correlation functional and norm conserving pseudopotentials were employed. For the large 270-atom supercells, the Kohn-Sham orbitals were

expanded in a triple-zeta-valence plus polarization (TZVP) Gaussian-type basis set and the charge density was expanded in a plane wave basis set with a cutoff of 100 Ry to efficiently solve the Poisson equation within the Quickstep scheme[20,21] as implemented in the CP2K suite of programs.[21] Brillouin zone integration was restricted to the supercell Γ point. Reference calculations for crystalline systems with small unit cells (see next section) were performed with a plane wave expansion of Kohn-Sham orbitals and Monkhorst-Pack (MP) meshes[22] for Brillouin zone integration as implemented in the Quantum Espresso suite of programs.[23] Phonons in the large cells were computed in Ref. 11 by diagonalizing the dynamical matrix obtained in turn from the variation of atomic forces due to finite atomic displacements 0.005 Å large. Only phonons with the periodicity of our supercell were considered. In the small systems, phonons were computed within density functional perturbation theory (DFPT).[24]

The BPM parameters were fitted to the *ab initio* Raman spectra of reference systems as discussed in Sec. III.

The differential cross section for Raman scattering (Stokes) in nonresonant conditions is given by (for a unit volume of scattering sample)

$$\frac{d^2\sigma}{d\Omega d\omega} = \sum_j \frac{\omega_S^4}{c^4} |\mathbf{e}_S \cdot \underline{\underline{R}}^j \cdot \mathbf{e}_L|^2 [n_B(\hbar\omega/k_bT) + 1]\delta(\omega - \omega_j), \tag{1}$$

where $n_B(\hbar\omega/k_bT)$ is the Bose factor, ω_S and ω_j are the frequencies of the scattered light and of the jth phonon, and $\mathbf{e}_S$ and $\mathbf{e}_L$ are the polarization vectors of the scattered and incident light, respectively. The Raman tensor $\underline{\underline{R}}^j$ associated with the jth phonon is given by

$$R^j_{\alpha\beta} = \sqrt{\frac{V_0\hbar}{2\omega_j}} \sum_{\kappa=1}^{N} \frac{\partial \chi^\infty_{\alpha\beta}}{\partial \mathbf{r}(\kappa)} \cdot \frac{\mathbf{e}(j,\kappa)}{\sqrt{M_\kappa}}, \tag{2}$$

where V_0 is the unit cell volume, $\mathbf{r}(\kappa)$ is the position of the κth atom of mass M_κ, ω_j and $\mathbf{e}(j,\kappa)$ are the frequency and eigenvector of the jth phonon, and $\underline{\underline{\chi}}^\infty = (\underline{\underline{\varepsilon}}^\infty - \mathbf{1})/4\pi$ is the electronic susceptibility. The BPM parameters were fitted on Raman tensors of selected systems computed within DFPT[24] as implemented in the Quantum Espresso suite of programs.[23] The derivatives of $\underline{\underline{\chi}}^\infty$ were computed by finite differences, by moving the atoms independently by symmetry with a maximum displacement of 0.01 Å.

The Raman cross sections for polarized HV and VV spectra are computed from Eq. (1) with the substitutions

$$2\left(R^2_{xx} + R^2_{yy} + R^2_{zz}\right) + 6\left(R^2_{xy} + R^2_{xz} + R^2_{yz}\right) - 2(R_{xx}R_{yy} + R_{xx}R_{zz} + R_{zz}R_{yy}) \to 15\pi |\mathbf{e}_S \cdot \mathbf{R}^j \cdot \mathbf{e}_L|^2 \tag{3}$$

and

$$6\left(R^2_{xx} + R^2_{yy} + R^2_{zz}\right) + 8\left(R^2_{xy} + R^2_{xz} + R^2_{yz}\right) + 4(R_{xx}R_{yy} + R_{xx}R_{zz} + R_{zz}R_{yy}) \to 15\pi |\mathbf{e}_S \cdot \mathbf{R}^j \cdot \mathbf{e}_L|^2, \tag{4}$$

respectively. The total Raman cross section for unpolarized light in backscattering geometry averaged over all possible incident directions is computed from Eq. (1), with the substitution

$$4\left(R^2_{xx} + R^2_{yy} + R^2_{zz}\right) + 7\left(R^2_{xy} + R^2_{xz} + R^2_{yz}\right) + (R_{xx}R_{yy} + R_{xx}R_{zz} + R_{zz}R_{yy}) \to 30|\mathbf{e}_S \cdot \mathbf{R}^j \cdot \mathbf{e}_L|^2. \tag{5}$$

III. FITTING THE BPM PARAMETERS

Within the BPM, the electronic susceptibility $\underline{\underline{\chi}}^\infty$ in Eq. (2) is written as a sum of bond polarizabilities α_β as $\alpha_{\beta,ij} = \alpha_{\beta\parallel}\hat{d}_{\beta,i}\hat{d}_{\beta,j} + \alpha_{\beta\perp}(\delta_{ij} - \hat{d}_{\beta,i}\hat{d}_{\beta,j})$, where $\hat{\mathbf{d}}_\beta$ is a unit vector which defines the direction of bond β, whose longitudinal and perpendicular polarizabilities are given by $\alpha_{\beta\parallel}$ and $\alpha_{\beta\perp}$. By assuming that the polarizabilities depend on bond lengths only, the Raman tensors within the BPM are defined by the parameter $\alpha_{\beta\parallel} - \alpha_{\beta\perp}$ and the derivatives with respect to the bond length $\alpha'_{\beta\parallel}$ and $\alpha'_{\beta\perp}$ for each type of bond β. To set up a BPM suitable to reproduce the Raman spectrum of GST, several types of bonds must be considered. The BPM parameters for the Sb-Te bond were fitted on the *ab initio* Raman spectrum of crystalline Sb_2Te_3 reported in Ref. 25. Two different sets of BPM parameters for the longer (3.17 Å) and shorter (2.97 Å) Sb-Te bonds present in crystalline Sb_2Te_3 turned out to be necessary to reproduce the Raman spectrum of crystalline Sb_2Te_3.[25] The BPM and *ab initio* Raman spectra of crystalline Sb_2Te_3 are compared in Fig. 1. The BPM parameter for the Ge-Te bond was fitted on the *ab initio* Raman tensors of crystalline hexagonal GST (hex-GST) reported in Ref. 26 in the stacking named A in which there is just a single Ge-Te bond length as proposed by Kooi and De Hosson.[27] The same parameters reproduce well also the Raman spectrum of stacking B in which two different Ge-Te bond lengths (2.83 and 3.22 Å[26]) are present as proposed by Petrov *et al.*[28] The BPM and *ab initio* Raman spectra of crystalline hex-GST in the two stackings are compared in Fig. 2.

In these calculations, we neglected the polarizability of Te-Te weak bonds. By including the polarizability of these latter bonds with all the other BPM parameters fixed, the

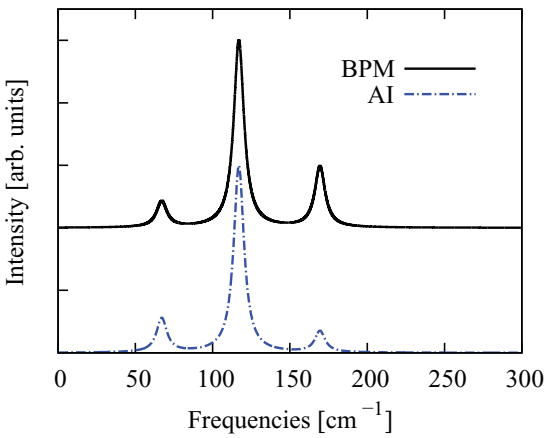

FIG. 1. (Color online) Raman spectrum of crystalline Sb_2Te_3 computed within the BPM (continuous line) and *ab initio* from Ref. 25 (dashed line).

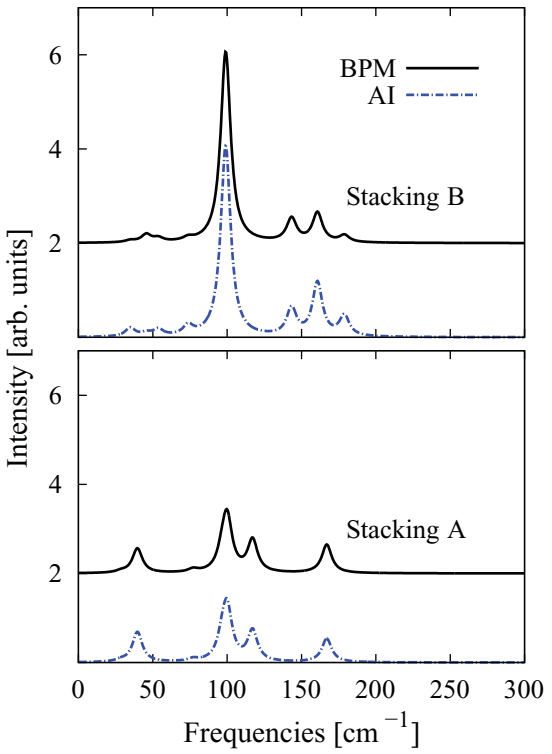

FIG. 2. (Color online) Raman spectrum of hexagonal GST computed within the BPM (continuous line) and *ab initio* from Ref. 26 (dashed line). We considered the two different stackings of the Ge-Sb planes named stacking A and B in Ref. 26 which correspond to the structures proposed in Ref. 27 and Ref. 28, respectively.

Raman spectra of crystalline Sb_2Te_3 and hex-GST in the two stackings improve only marginally. As a further check of the transferability of the BPM model we computed the *ab initio* Raman spectrum of a seven-atom NaCl-like cell of $GeSb_2Te_4$ [Te on one sublattice, Ge, Sb, and a vacancy on the other sublattice at the theoretical lattice parameter (6.14 Å) and with a 16×16×16 Monkhorst-Pack mesh[22]]. The *ab initio* and BPM spectra of $GeSb_2Te_4$ are compared in Fig. 3. Minor discrepancies are present due to the constitutional vacancies which introduce a larger spread in the bond lengths

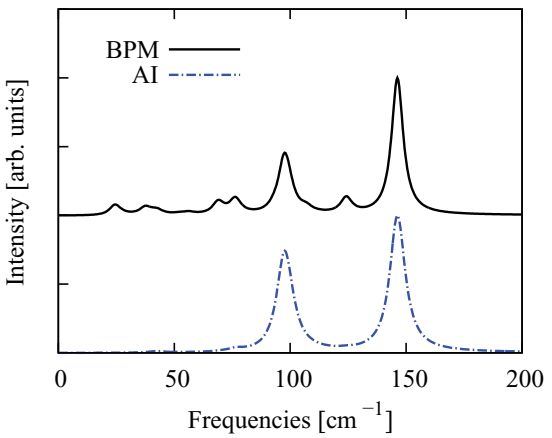

FIG. 3. (Color online) Raman spectrum of a small cell of $GeSb_2Te_4$ within the BPM (continuous line) and *ab initio* (dashed line).

of $GeSb_2Te_4$ with respect to hex-GST. This spread is further enhanced by the small size of the simulation cell we used; it reduces the transferability of the BPM parameters fitted on hex-GST which is, however, overall acceptable. Thus, we used the BPM parameters fitted on hexagonal Sb_2Te_3 and hex-GST for the Raman spectrum of cubic GST.

However, the BPM parameters of the Ge-Te bond in hex-GST turned out to be much larger (roughly a factor three) than the parameters for the Ge-Te bond obtained in our previous work[15] on the Raman spectra of amorphous GeTe. This outcome is presumably a manifestation of the presence of resonating valence bonds in hexagonal and cubic GST, which are responsible for an enhancement of the dielectric function in the crystalline phase with respect to the amorphous phases of GST and GeTe.[29–31] For amorphous GST we thus used the same BPM parameters for the Ge-Te bonds developed previously for amorphous GeTe.[15] Moreover, different types of Ge-Ge and Ge-Te bonds are present in a-GST for which we used the same BPM parameters obtained in Ref. 15 for a-GeTe, namely Ge(tetra)-Ge(tetra), Ge(tetra)-Ge(octa), Ge(octa)-Ge(octa), Ge(tetra)-Te and Ge(octa)-Te. Since the spectrum of the a-GeTe was very weakly dependent on the parameters for the Ge(tetra)-Ge(tetra) bond, they were fixed to those of crystalline Ge.[32] For Sb-Sb and Sb-Ge bonds in a-GST we considered an antisite defect in Sb_2Te_3 and a substitutional Sb_{Ge} defect in α-GeTe, respectively. In these latter cases, the BPM parameters were fitted on the derivatives of the electronic susceptibilities with respect to the position of the defect atoms. Supercells with 16 or 32 atoms were used.

The full set of best-fit BPM parameters is reported in Table I. A summary of the choices of the BPM parameters we made for the study of c-GST and a-GST is given in the caption of

TABLE I. Best-fit polarizability parameters (atomic units) of the bond polarizability model. "Tetra" indicates tetrahedral Ge and "octa" octahedral Ge. Ge-Sb parameters are taken equal for tetrahedral and octahedral Ge. For amorphous GST, we used the Ge-Te parameters indicated by a-GST that we obtained in our previous work[15] by fitting the Raman spectra of crystalline and amorphous GeTe. For cubic GST, we used the Ge-Te parameters indicated by c-GST that we fitted on the Raman spectrum of hexagonal GST. The two sets of Sb-Te parameters for long and short bonds were fitted on the Raman spectrum of crystalline Sb_2Te_3. The parameters for Ge(tetra)-Ge(tetra) are those of crystalline Ge from Ref. 32. All the other Ge-Ge parameters were fitted on the Raman spectra of amorphous GeTe in Ref. 15. The Sb-Sb and Ge-Sb parameters were obtained from defects in crystalline Sb_2Te_3 and GeTe.

Bond	$\alpha_\parallel - \alpha_\perp$	$\alpha'_\parallel$	$\alpha'_\perp$
Ge(tetra)-Ge(tetra)	−6.8	50.0	15.6
Ge(tetra)-Ge(octa)	−17.2	76.5	51.0
Ge(octa)-Ge(octa)	−34.4	41.1	10.4
Ge(tetra)-Te	103.1	96.8	75.0
Ge(octa)-Te (a-GST)	61.9	37.0	17.7
Ge(octa)-Te (c-GST)	233.8	139.2	69.3
Sb-Te (short bonds)	331.8	492.2	16.8
Sb-Te (long bonds)	137.7	177.5	73.0
Sb-Sb	−220.2	190.5	256.3
Ge-Sb	59.8	58.4	140.5

Table I. The resonating valence bonds discussed in Refs. 29–31 are present also in crystalline Sb_2Te_3 and are presumably responsible for the anomalously large BPM parameters for Sb-Te bonds as compared for instance to the atomic polarizability of Sb (42 a.u. in Ref. 33).

IV. RESULTS

A. Structural properties

We here report some data on the structural properties of a-GST in addition to those presented in Refs. 10,11. In the amorphous phase, Ge and Sb atoms are mostly fourfold coordinated, while Te atoms are mostly threefold coordinated. All Te and Sb and 73% of Ge atoms are in a defective octahedral-like geometry with octahedral bonding angles but a lower than six coordination (see inset of Fig. 4). Actually, the distribution of the bond lengths for Ge and Sb atoms in octahedral-like sites reported in Fig. 4 shows a bimodal distribution which becomes more evident in Fig. 5, where

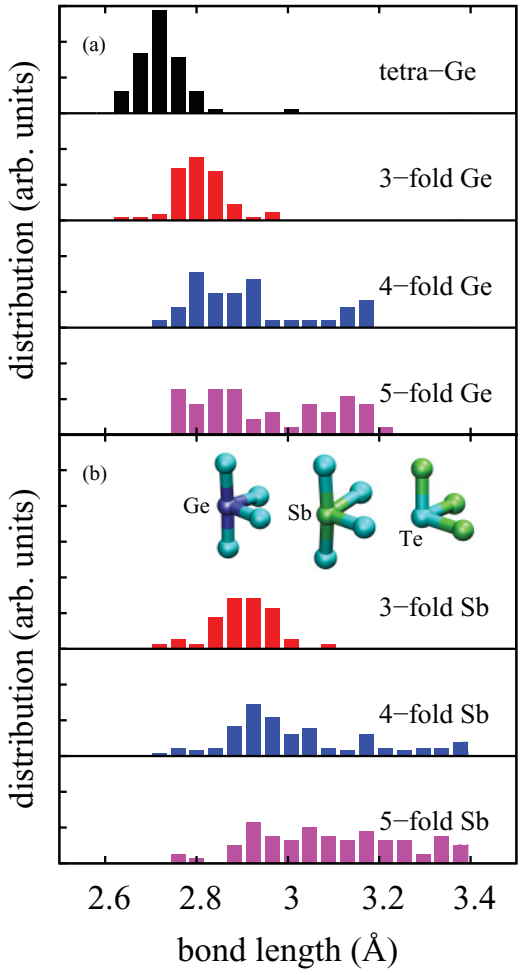

FIG. 4. (Color online) Distribution of bond lengths for (a) Ge in tetrahedral (tetra) and defective octahedral sites and for (b) Sb with different coordination in a-GST. Inset: Sketch of the most frequent local geometries in a-GST corresponding to defective octahedral sites of 4-coordinated Ge and Sb and 3-coordinated Te.[10,11]

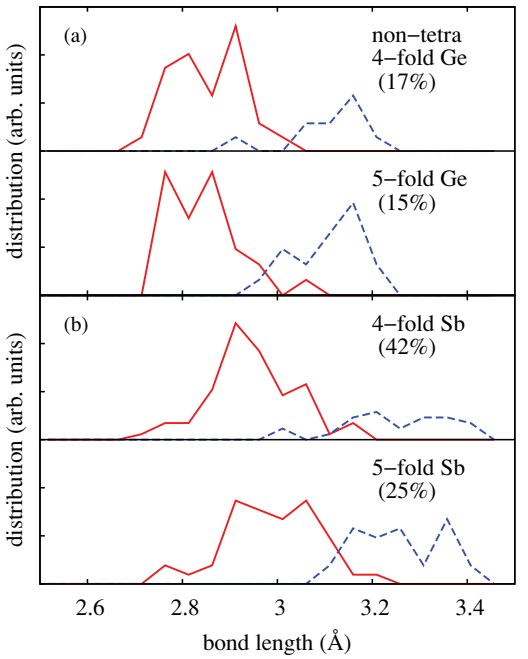

FIG. 5. (Color online) Distribution of the three shorter (continuous line) and the other, longer (dashed) bond lengths for (a) Ge and (b) Sb in defective octahedral sites with different coordination in a-GST.

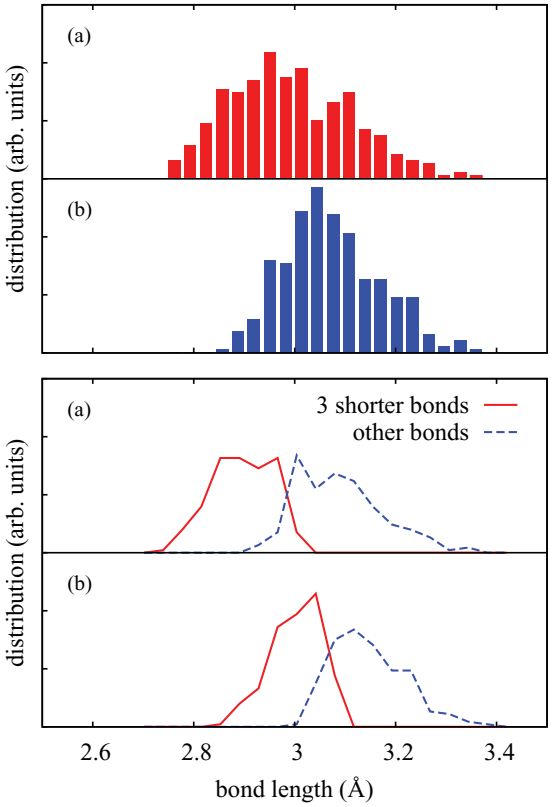

FIG. 6. (Color online) Upper panel: Distribution of bond lengths for (a) Ge and (b) Sb in cubic GST. Lower panel: Distribution of the three shorter (continuous line) and the other, longer (dashed) bond lengths for (a) Ge and (b) Sb in cubic GST.

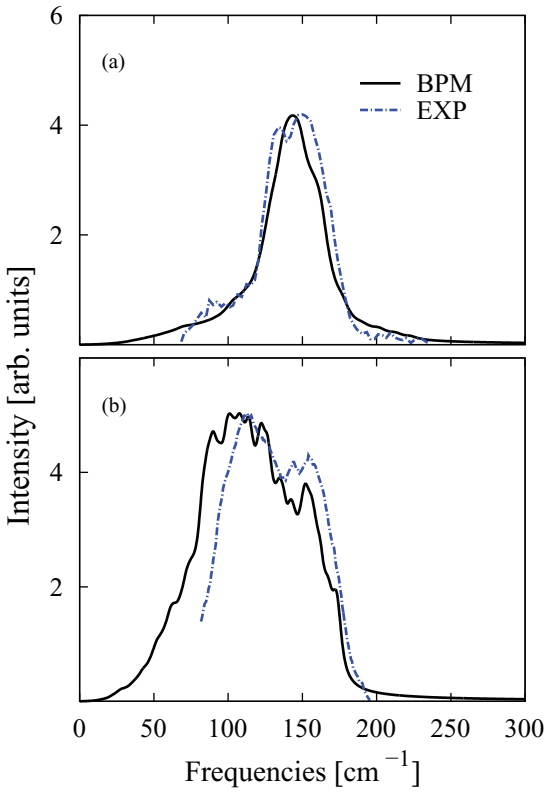

FIG. 7. (Color online) Reduced Raman spectrum of (a) a-GST and (b) crystalline c-GST, computed within the BPM (continuous line) for unpolarized light in backscattering geometry compared with the analogous experimental spectra (dashed line) from Ref. 5. The reduced spectrum is obtained by multiplying by $\omega_S^{-4}\omega^1(n_B+1)^{-1}$ the Raman scattering (Stokes) cross section given in Eq. (1). The theoretical spectra are obtained by substituting the δ functions in Eq. (1) with Lorentzian functions 5 cm^{-1} wide. We averaged over all possible incident directions of the light as in Eq. (5).

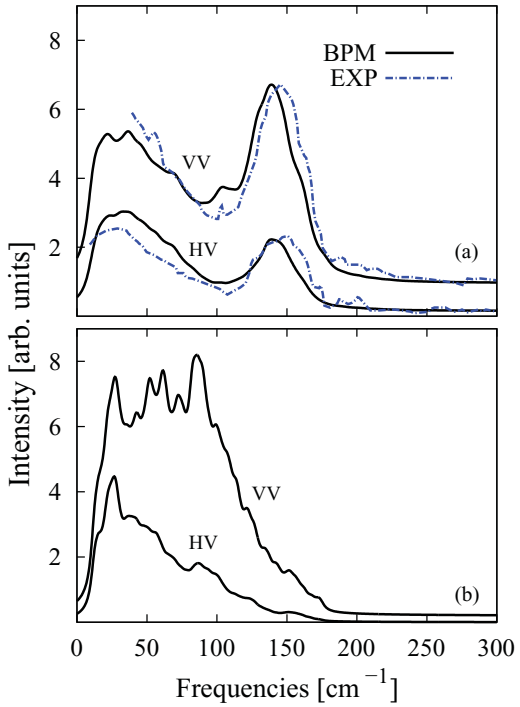

FIG. 8. (Color online) Raman spectra in HV and VV scattering geometries for (a) a-GST and (b) c-GST computed within the BPM (continuous line) and measured experimentally (dashed line, only for as-deposited a-GST) in Ref. 8.

the distribution is plotted for the three shorter bonds and for the longer ones. Therefore the defective octahedral-like environment of Ge/Sb recalls a $3+n$ ($n=0$–2) geometry similar to the $3+3$ bonding coordination in crystalline α-GeTe. These structures are ruled by the formation of p bonds as recently pointed out by Xu *et al.*[16] The same analysis in cubic GST shows a much less pronounced separation in longer and shorter bonds with respect to the amorphous phase as displayed in Fig. 6.

Some Ge atoms are tetrahedrally coordinated, as inferred from EXAFS data,[6] although only in the fraction of 27%.[11] The distribution of different tetrahedral units $GeTe_{4-n-m}Sb_mGe_n$ reported in Ref. 11 shows that the tetrahedral coordination of Ge is favored by homopolar Ge-Ge and Ge-Sb bonds.[10] This feature can be rationalized as follows. Ge is divalent in the defective octahedral sites and needs a dative bond from a lone pair of Te to complete the p shell.[16,34] In the lack of Te lone pairs due to the presence of wrong bonds, Ge cannot fill the p shell and then the s electrons are promoted into the valence forming sp^3 hybrids and turning the defective octahedra into tetrahedra. Finally, there are no chains of Te atoms but a few dimers and trimers.

B. Vibrational properties and Raman spectra

Phonon densities of states (DOS) of the models of a-GST and c-GST at the supercell Γ point have been reported in our previous work.[11] The analysis of the localization properties of the phonons in Ref. 11 revealed that phonons above 190 cm^{-1} in a-GST are mostly localized on tetrahedral sites as occurs in a-GeTe.[15] These strongly localized modes give rise to a high-frequency tail in the DOS of a-GST which extends above the highest frequency of the DOS of c-GST.[11]

The Raman spectra of c-GST and a-GST computed with the best-fit BPM parameters (Table I) are compared in Fig. 7 to the experimental Raman spectra of c-GST and as-deposited a-GST.[5] The theoretical polarized spectra in HV and VV geometries are compared with experimental data from as-deposited a-GST[8] in Fig. 8.

The main features of the experimental Raman spectra are well reproduced by theory. In the experimental Raman spectrum of c-GST we recognize two main structures, one at 110 cm^{-1} and a second weaker structure at 160 cm^{-1} while the spectrum of a-GST shows two peaks at 129 cm^{-1} and 152 cm^{-1} and much weaker structures around 100 cm^{-1}. The theoretical Raman spectrum of a-GST shows a peak at $\sim$143 cm^{-1} and a shoulder at 160 cm^{-1}. These (slight) misfits could have different sources. First, as opposed to experiments, our spectrum is computed in nonresonant conditions. Second, the limited statistics accessible by our still small simulation cell might weight differently the contributions from different local structures as shown in Fig. 9 in which we compare the Raman spectrum of the 270-atom model with that of a larger 297-atom model generated in a similar way. Finally, further discrepancies might come from the fact that the experimental

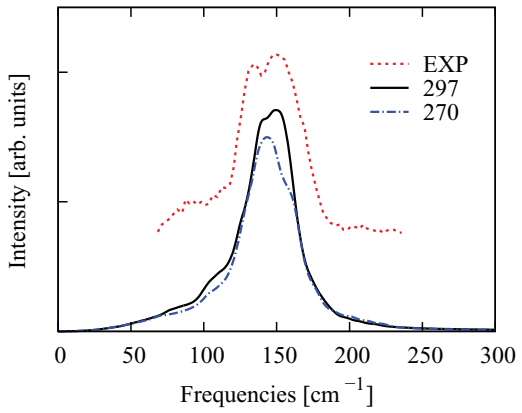

FIG. 9. (Color online) Comparison of the experimental (Ref. 5) and theoretical reduced Raman spectra for two different models of a-GST, 270 atoms and 297 atoms large.

spectrum we compare with is recorded on as-deposited a-GST while our model is generated by quenching from the melt. However, possible different concentrations of Ge tetrahedra in the melt-quenched and as-deposited amorphous phases[35] cannot be detected by Raman spectroscopy, since the Raman spectrum of GST is dominated by vibrations of the more polarizable Sb-Te bonds, as discussed below.

Insight on the phonons responsible for the different Raman peaks is gained from the analysis of the reduced Raman spectra projected on different types of atoms reported in Figs. 10 and 11. These projections and those discussed later on are obtained by multiplying the Raman cross section for each individual

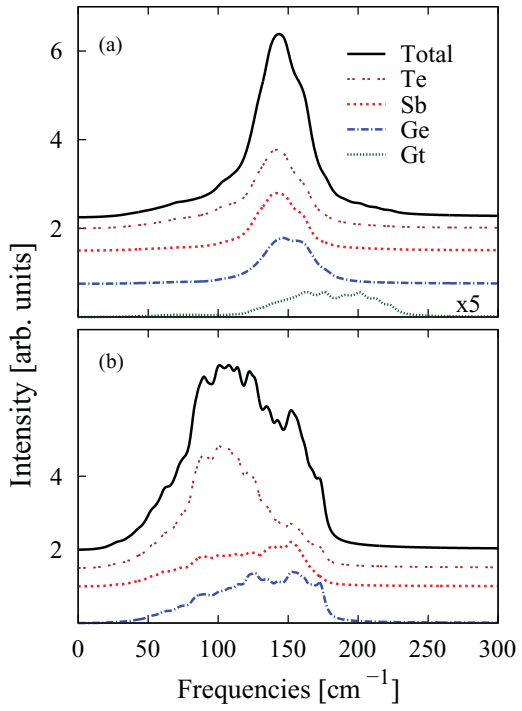

FIG. 10. (Color online) Projection of the reduced Raman spectrum in Fig. 7 on different types of atoms for (a) a-GST and (b) c-GST. Gt indicates tetrahedral germanium and Ge octahedral-like germanium.

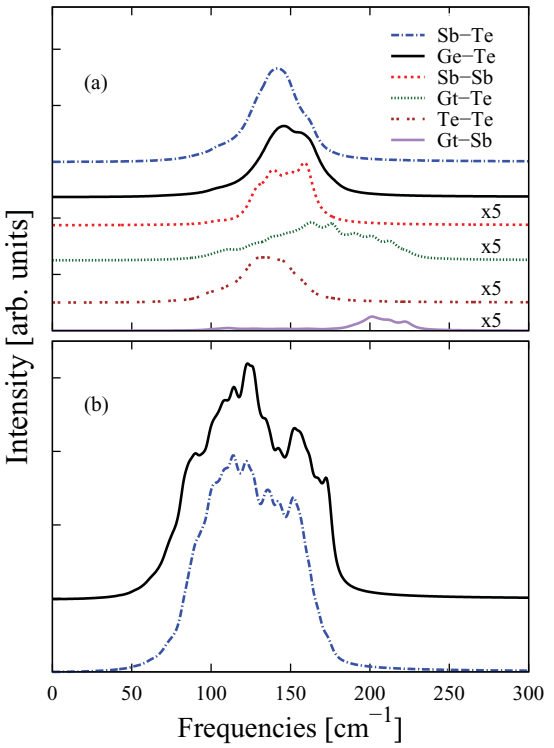

FIG. 11. (Color online) Projection of the reduced Raman spectra in Fig. 7 on different types of bonds for (a) a-GST and (b) c-GST. Gt indicates tetrahedral germanium and Ge octahedral-like germanium.

phonon in the sum of Eq. (1) by suitable projections of the corresponding eigenvector, e.g., by $\sum_\kappa \frac{|e(j,\kappa)|^2}{M_\kappa}$ where the sum is restricted to atoms of a single species for the spectra in Fig. 10. The peak at 143 cm^{-1} and the shoulder at 160 cm^{-1} are both due to vibrations of defective octahedra. As opposed to a-GeTe, Ge tetrahedra do not show up in the Raman spectrum of a-GST. This is not due to the lack of tetrahedral sites which do contribute to the tail of the DOS similarly in a-GST and a-GeTe.[11,15] However, as opposed to a-GeTe, the Raman cross section is much weaker for tetrahedra than for octahedra in a-GST. This is due to the fact that the most intense peaks in a-GST are dominated by modulations of the Sb-Te bonds in defective octahedra which are much more polarizable than Ge-Te bonds. This is demonstrated in Fig. 12, which shows the Raman spectrum of a-GST computed by setting the BPM parameters of Sb-Te bonds equal to those of the Ge-Te bond for defective octahedra in Table I. As a result, the Raman signatures of Ge tetrahedra are not visible in the experimental Raman spectrum of a-GST. We also computed the Raman spectrum of amorphous Sb_2Te_3 (a-Sb_2Te_3) with the same BPM parameters used for a-GST and phonons from the *ab initio* model of a-Sb_2Te_3 which contains only defective octahedra presented in Ref. 36 (cf. Fig. 13). The spectrum of a-Sb_2Te_3 is similar to that of a-GST, which further confirms that Sb-Te bonds of defective octahedra dominate the spectrum of a-GST.

The theoretical spectra also reproduce a surprising feature of the experimental data, namely the fact that, as opposed to the common behavior of most materials, the Raman spectrum of the crystalline phase is broader than the spectrum of the amorphous phase. This is due to the presence of disorder in

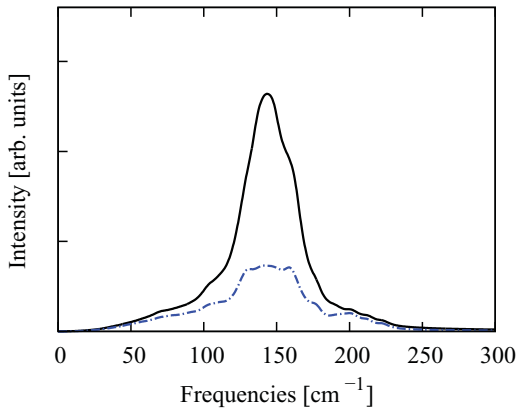

FIG. 12. (Color online) Reduced Raman spectrum of a-GST in Fig. 7 (continuous line) compared with the spectrum computed by setting the BPM parameters of the Sb-Te bonds equal to those of the Ge-Te bond (cf. Table I) (dashed line).

the form of 20% of vacancy sites in one sublattice of c-GST. As reported in our previous work, vacancies induce a large atomic relaxation with a broad distribution in Ge-Te (Fig. 22 in Ref. 11) and Sb-Te bond lengths. The spread in Ge-Te and Sb-Te bond lengths is actually larger in c-GST than in a-GST where, in the lack of symmetry constraints, atoms relax more easily toward the optimal length for p-type bonds in agreement with EXAFS data.[6] Still, a-GST is higher in energy than c-GST due to the lack of medium range order already at the level of second-nearest neighbor which is responsible for the loss of resonating valence bonding according to the picture introduced in Ref. 29. The larger spread in the bond lengths of c-GST with respect to a-GST shows up in a larger full width at half maximum of the pair correlation functions (Ge-Te and Sb-Te) reported in Fig. 4 of Ref. 11. A larger spread in bond lengths results into a larger spread in the force constants controlling the Raman active modes.

As discussed in Sec. IV A, three Ge-Te or Sb-Te bonds are shorter than the others giving rise to a $3 + n$ coordination in the defective octahedra. Thus in the topology of a-GST

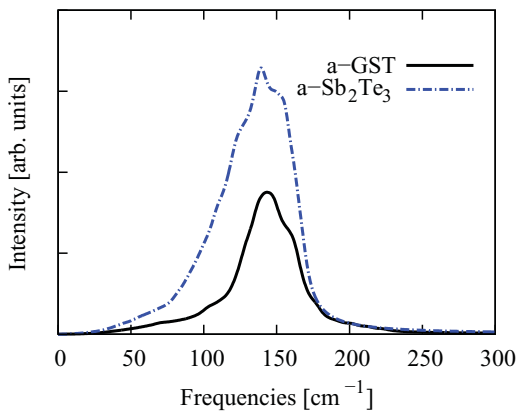

FIG. 13. (Color online) Theoretical reduced Raman spectrum of a-GST and a-Sb_2Te_3 (see text) computed with the BPM model for unpolarized light in backscattering geometry. The calculation details are the same as those provided in the caption of Fig. 7.

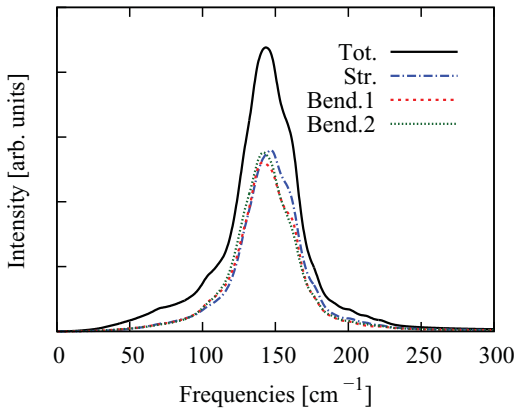

FIG. 14. (Color online) Total projections of the reduced Raman spectrum on bending- and stretching-like displacements of atoms in pyramidal units. The projections were obtained by summing up the contributions of all the structural units. Total refers to the original Raman spectrum. The sum of the projections is not normalized to the total spectrum because of double counting (e.g., a Te atom belongs to a few $GeTe_3$ units). The projection on stretching-like modes is defined as the projection on displacements of each Ge/Sb and Te along the direction defined by the height of the $Te(Ge/Sb)_3$ and $(Ge/Sb)Te_{3-n}(Ge/Sb)_n$ pyramids [e.g., the direction $\sum_i \mathbf{x}(\mathrm{Te}) - \mathbf{x}((\mathrm{Ge/Sb})_i)$ for the $Te(Ge/Sb)_3$ unit]. The projection on bending-like modes is defined as the projection of displacements of each Ge/Sb and Te atom on the two directions perpendicular to the stretching direction defined above.

one can recognize $Te(Ge/Sb)_3$ units and analogous units made of $(Ge/Sb)Te_{3-n}(Ge/Sb)_n$ ($n = 0$–2) plus one or two longer bonds similar to those present in crystalline α-GeTe. However, the misalignment of four-membered rings in a-GST prevents a classification of normal modes in bending and stretching modes of the pyramidal units such as the E and A_1 modes of α-GeTe. Nevertheless, the projection of the Raman spectrum of a-GST on bending- and stretching-like displacements of the pyramidal units reported in Fig. 14 shows that the shoulder at 160 cm^{-1} is mostly due to stretching-like modes.

V. CONCLUSIONS

Based on *ab initio* calculations we have provided an assignment of the Raman spectrum of a-GST and c-GST to vibrations of the specific local structures. The good agreement with the experimental spectra provides further evidence of the validity of the structural model of the amorphous phase generated by quenching from the melt within first-principles molecular dynamics simulations. Inspection on the phonon displacements reveals that the main Raman peaks at 110 and 160 cm^{-1} in c-GST and the two peaks at 129 and 152 cm^{-1} in a-GST are due to vibrations of defective octahedra. Although in a-GST the phonon density of states above 190 cm^{-1} is dominated by vibrations strongly localized on tetrahedra, they do not show up in Raman spectra because of the much lower polarizability of Ge-Te and Ge-Ge/Sb bonds present in tetrahedra with respect to the Sb-Te bonds in defective octahedra. As opposed to amorphous GeTe,[15] the signatures of tetrahedra in the Raman spectrum of amorphous GST are hidden by the larger Raman cross

section of vibrations of defective octahedra. In agreement with this finding, the Raman spectrum of amorphous Sb_2Te_3 is very similar to the spectrum of a-GST. As opposed to the common behavior of most materials, the Raman spectrum of the crystalline cubic GST phase is broader than the spectrum of the amorphous phase. This is due to the presence of disorder in the form of 20% of vacancy sites in one sublattice of c-GST, which makes the spread in Ge-Te and Sb-Te bond lengths larger in c-GST than in a-GST.[6,11]

ACKNOWLEDGMENTS

We thankfully acknowledge the computational resources by DEISA Consortium under projects PHASEMAT and PHASEALL and by CSCS (Manno, Switzerland). This work is partially supported by the Cariplo Foundation through project Monads and by MURST through the program Prin08. S.C. acknowledges support through SNSF (Contract No. 200021-119882). We gratefully acknowledge E. Rimini, E. Carria, and M. G. Grimaldi for discussions and information.

*marco.bernasconi@unimib.it

[1] M. Wuttig and N. Yamada, Nature Mater. **6**, 824 (2007).

[2] A. Pirovano, A. L. Lacaita, A. Benvenuti, F. Pellizzer, and R. Bez, IEEE Trans. Electron. Devices **51**, 452 (2004).

[3] A. L. Lacaita and D. J. Wouters, Phys. Status Solidi A **205**, 2281 (2008).

[4] W. Weidenhof, I. Friedrich, S. Ziegler, and M. Wuttig, J. Appl. Phys. **89**, 3168 (2001).

[5] R. De Bastiani, A. M. Piro, M. G. Grimaldi, E. Rimini, G. A. Baratta, and G. Strazzulla, Appl. Phys. Lett. **92**, 241925 (2008).

[6] A. V. Kolobov, P. Fons, A. I. Frenkel, A. L. Ankudinov, J. Tominaga, and T. Uruga, Nature Mater. **3**, 703 (2004).

[7] A. V. Kolobov, P. Fons, and J. Tominaga, Appl. Phys. Lett. **82**, 382 (2003).

[8] K. S. Andrikopoulos, S. N. Yannopoulos, A. V. Kolobov, P. Fons, and J. Tominaga, J. Phys. Chem. Sol. **68**, 1074 (2007).

[9] K. S. Andrikopoulos, S. N. Yannopoulos, G. A. Voyiatzis, A. V. Kolobov, M. Ribes, and J. Tominaga, J. Phys. Condens. Matter **18**, 965 (2006).

[10] S. Caravati, M. Bernasconi, T. D. Kühne, M. Krack, and M. Parrinello, Appl. Phys. Lett. **91**, 171906 (2007).

[11] S. Caravati, M. Bernasconi, T. D. Kühne, M. Krack, and M. Parrinello, J. Phys. Condens. Matter **21**, 255501 (2009); *ibid*. **21**, 499803 (2009); S. Caravati, M. Bernasconi, T. D. Kühne, M. Krack, and M. Parrinello, *ibid*. **22**, 399801 (2010).

[12] S. Caravati, M. Bernasconi, and M. Parrinello, J. Phys. Condens. Matter **22**, 315801 (2010).

[13] J. Akola and R. O. Jones, Phys. Rev. B **76**, 235201 (2007); Phys. Rev. Lett. **100**, 205502 (2008).

[14] J. Akola, R. O. Jones, S. Kohara, S. Kimura, K. Kobayashi, M. Takata, T. Matsunaga, R. Kojima, and N. Yamada, Phys. Rev. B **80**, 020201(R) (2009).

[15] R. Mazzarello, S. Caravati, S. Angioletti-Uberti, M. Bernasconi, and M. Parrinello, Phys. Rev. Lett. **104**, 085503 (2010).

[16] M. Xu, Y. Q. Cheng, H. W. Sheng, and E. Ma, Phys. Rev. Lett. **103**, 195502 (2009).

[17] T. Matsunaga, N. Yamada, and Y. Kubota, Acta Crystallogr. B **60**, 685 (2004).

[18] M. V. Wolkenstein, C. R. Acad. Sci. URSS **30**, 791 (1941); M. A. Eliashevich and M. V. Wolkenstein, J. Phys. (USSR) **9**, 101 (1944).

[19] J. P. Perdew, K. Burke, and M. Ernzerhof, Phys. Rev. Lett. **77**, 3865 (1996).

[20] M. Krack and M. Parrinello, in *High Performance Computing in Chemistry*, edited by J. Grotendorst (NIC, Jülich, 2004), Vol. 25, pp. 29-51; [http://cp2k.berlios.de].

[21] J. VandeVondele, M. Krack, F. Mohamed, M. Parrinello, T. Chassaing, and J. Hutter, Comput. Phys. Commun. **167**, 103 (2005).

[22] H. J. Monkhorst and J. D. Pack, Phys. Rev. B **13**, 5188 (1976).

[23] P. Giannozzi *et al*. J. Phys. Condens. Matter **21**, 395502 (2009); [http://www.quantum-espresso.org].

[24] S. Baroni, S. de Gironcoli, A. Dal Corso, and P. Giannozzi, Rev. Mod. Phys. **73**, 515 (2001).

[25] G. C. Sosso, S. Caravati, and M. Bernasconi, J. Phys. Condens. Matter **21**, 095410 (2009).

[26] G. C. Sosso, S. Caravati, C. Gatti, S. Assoni, and M. Bernasconi, J. Phys. Condens. Matter **21**, 245401 (2009).

[27] B. J. Kooi and T. M. J. De Hosson, J. Appl. Phys. **92**, 3584 (2002).

[28] I. I. Petrov, R. M. Imamov, and Z. G. Pinsker, Sov. Phys. Crystallogr. **13**, 339 (1968).

[29] K. Shportko, S. Kremers, M. Woda, D. Lencer, J. Robertson, and M. Wuttig, Nature Mater.**7**, 653 (2008).

[30] B. Huang and J. Robertson, Phys. Rev. B **81**, 081204(R) (2010).

[31] D. Lencer, M. Salinga, B. Grabowski, T. Hickel, J. Neugebauer, and M. Wuttig, Nature Mater.**7**, 972 (2008).

[32] S. Go, H. Bilz, and M. Cardona, Phys. Rev. Lett. **34**, 580 (1975).

[33] G. Maroulis, Chem. Phys. Lett. **444**, 44 (2007).

[34] M. H. Muser, Eur. Phys. J. B **74**, 291 (2010).

[35] J. Akola, J. Larrucea, and R. O. Jones, Phys. Rev. B **83**, 094113 (2011).

[36] S. Caravati, M. Bernasconi, and M. Parrinello, Phys. Rev. B **81**, 014201 (2010).